analytical chemistry

pubs.acs.org/ac

Article

Visualizing Dipeptidyl Peptidase-IV with an Advanced Non-π-Conjugated Fluorescent Probe for Early Thyroid Disease Diagnosis

Jiaxin Li, Mo Ma, Jingkang Li, Lanlan Xu, Daqian Song, Pinyi Ma,* and Qiang Fei*

Cite This: *Anal. Chem.* 2023, 95, 17577−17585

Read Online

ACCESS | Metrics & More | Article Recommendations | Supporting Information

ABSTRACT: Early detection and effective treatment of thyroid cancer are vital due to the aggressiveness and high mortality rate of the cancer. Nevertheless, the exploration of dipeptidyl peptidase-IV (DPP-IV) as a biomarker for thyroid diseases has not been widely conducted. In this study, we developed a novel non-π-conjugated near-infrared fluorescent probe, MB-DPP4, specifically designed to visualize and detect endogenous DPP-IV. Traditional DPP-IV-specific fluorescent probes rely primarily on the intramolecular charge transfer mechanism. For this reason, these probes are often hampered by high background levels that can inhibit their ability to achieve a fluorescence turn-on effect. MB-DPP4 successfully surmounts several drawbacks of traditional DPP-IV probes, boasting unique features such as exceptional selectivity, ultrahigh sensitivity (0.29 ng/mL), innovative structure, low background, and long-wavelength fluorescence. MB-DPP4 is an "off−on" chemosensor that exhibits strong fluorescence at 715 nm and releases a methylene blue (MB) fluorophore upon interacting with DPP-IV, resulting in a visible color change from colorless to blue. Given these remarkable attributes, MB-DPP4 shows great promise as a versatile tool for advancing research on biological processes and for evaluating the physiological roles of DPP-IV in living systems. Finally, we conducted a comprehensive investigation of DPP-IV expression in human serum, urine, thyroid cells, and mouse thyroid tumor models. Our findings could potentially establish a foundation for the early diagnosis and treatment of thyroid diseases.

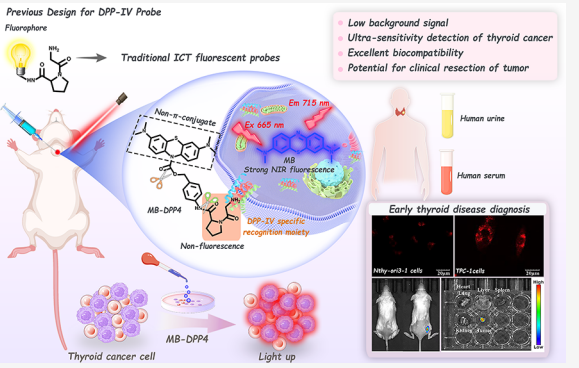

INTRODUCTION

Enzymes are increasingly recognized as potential biomarkers for tumors due to their integral role in various physiological, pathological, and pharmacological processes that are pertinent to tumor diagnosis and treatment.[1,2] One such enzyme, dipeptidyl peptidase-IV (DPP-IV, E.C 3.4.14.5), also known as CD26, belongs to the dipeptidyl peptidase family.[3] As a serine protease, DPP-IV exhibits proteolytic activity and functions as a transmembrane glycoprotein that efficiently degrades N-terminal dipeptides from polypeptides when proline or alanine is in the penultimate position.[4,5] DPP-IV is ubiquitously expressed across a wide range of cells, tissues, and organs.[6,7] This extensive presence, coupled with its proteolytic activity, significantly impacts numerous physiological and pathological processes, such as endocrine function, glucose metabolism/homeostasis, and autoimmunity.[8,9] Given its diverse roles in many biological processes, DPP-IV has become an appealing new biomarker in numerous fields, especially in tumor biology.[10−13]

Thyroid cancer is the most common form of endocrine malignancy that has seen a significant rise in incidence rates in recent decades.[14−16] Some studies have reported an elevation in the expression of DPP-IV—a biomarker for malignancy in thyroid nodules and thyroid cancers.[17−20] Imaging remains the most effective diagnostic method for significant human lesions; thus, we have developed a new method for the diagnosis of thyroid nodular lesions, which challenges conventional imaging or needle biopsy.[21,22] Typically, confirming a diagnosis requires several days of extensive pathological examination, and the process is laborious and heavily reliant on the pathologist's subjective judgment.[23] In recent years, near-infrared (NIR) fluorescent probes have been proven particularly valuable in identifying and imaging biomolecules owing to their high tissue penetration and the ability to bypass autofluorescence; thus, they have become the tools widely used in disease diagnosis and treatment.[24−29]

Therefore, the development of a novel DPP-IV-specific fluorescent probe is essential for the early diagnosis of thyroid diseases.[30] Existing DPP-IV-specific fluorescent probes have been used mainly in the context of diabetes and liver cancer, but the use for exploring DPP-IV expression levels in thyroid diseases via fluorescence imaging has not been conducted.[31−33]

Received: July 3, 2023
Revised: October 12, 2023
Accepted: November 8, 2023
Published: November 21, 2023

https://doi.org/10.1021/acs.analchem.3c02909
Anal. Chem. 2023, 95, 17577−17585

Scheme 1. Synthetic Route of Probe MB-DPP4

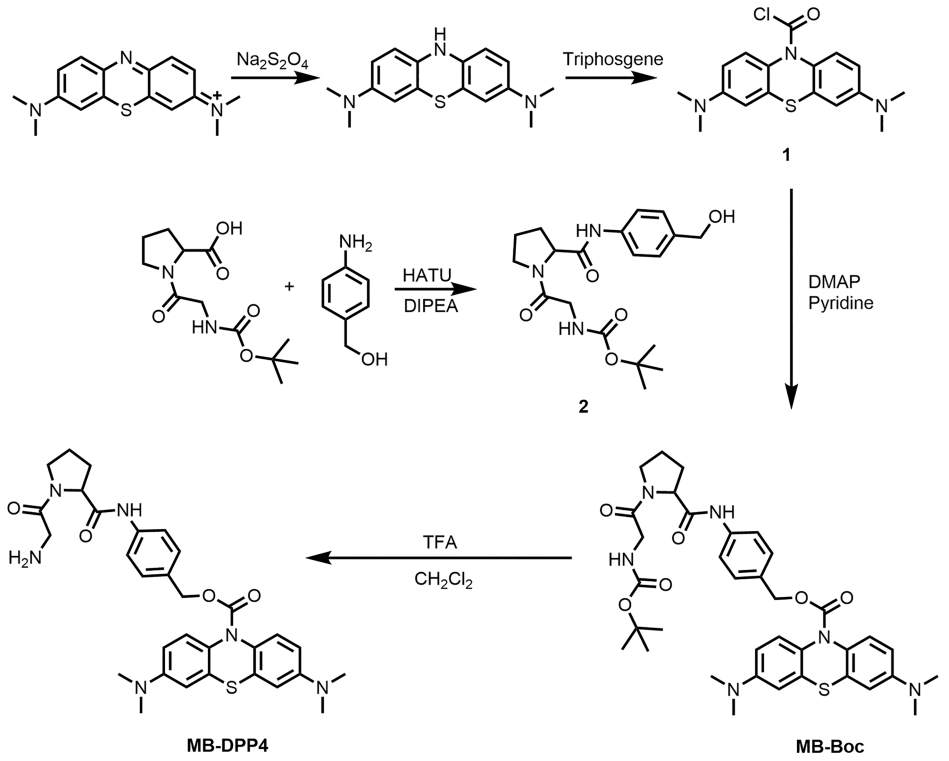

Moreover, the current design strategy for DPP-IV fluorescent probes primarily relies on the intramolecular charge transfer (ICT) mechanism but fails to address the effective quenching of the background signal.[33−35]

In this study, we designed a novel non-π-conjugated NIR fluorescent probe, MB-DPP4, to detect DPP-IV activity in thyroid cancer and used it for visual biofluorescence imaging (Scheme 1). The probe was based on a methylene blue (MB) fluorophore and was synthesized by disrupting its conjugated structure and by introducing a self-dissociating linker group along with a DPP-IV recognition element. This strategy resulted in a low background signal, allowing the probe to have a high sensitivity to DPP-IV. After its fluorescence performance and recognition mechanism were systematically investigated, MB-DPP4 was further applied to detect DPP-IV in human serum, urine, thyroid cells, and mouse thyroid tumor models. This research not only introduces a highly sensitive DPP-IV-specific fluorescent probe but also presents a novel design strategy for fluorescent probes that can potentially achieve the unprecedented detection of a variety of enzymes and other biologically active analytes due to its low background fluorescence switch response.

EXPERIMENTAL PROCEDURE

Materials and Instruments. Relevant reagents and apparatus can be found in the Supporting Information.

Synthesis of Compound 1. Under a nitrogen atmosphere, methylene blue (0.16 g, 0.5 mmol) and sodium carbonate (0.2 g, 2.0 mmol) were dissolved in 7.0 mL of water. Subsequently, 6.0 mL of CH_2Cl_2 was added to the solution. After sodium dithionite (0.4 g, 2.0 mmol), dissolved in 10.0 mL of water, was slowly added, the mixture was stirred at 40 °C for 1 h until its color changed to a yellow color. After that, triethylamine (100 μL, 0.7 mmol) was added dropwise, and the reaction mixture was cooled to below 0 °C. Triphosgene (0.1 g, 0.3 mmol), dissolved in 5 mL of CH_2Cl_2, was subsequently added dropwise to the reaction mixture, which was then further stirred at 40 °C under a nitrogen atmosphere for 1 h. The completion of the reaction was confirmed by thin-layer chromatography (TLC). The solvent was cooled to room temperature, and the upper aqueous phase of the mixture was removed under a closed system, leaving the CH_2Cl_2 organic layer. This organic layer was used directly in a subsequent step without purification.

Synthesis of Compound 2. Boc-Gly-Pro-OH (0.27 g, 1 mmol), HATU (0.38 g, 1 mmol), and DIPEA (0.18 mL, 1 mmol) were mixed with 5 mL of anhydrous THF and then stirred for 10 min at 0 °C. Subsequently, 4-aminobenzyl alcohol (0.12 g, 2 mmol), dissolved in 1 mL of anhydrous THF, was added dropwise into the mixture. The reaction mixture was stirred at 0 °C for 10 min and then at room temperature for 5 h. The progress of the reaction was monitored by TLC until completion. Afterward, the solvent was evaporated under vacuum, and the remaining crude product was purified by silica gel column chromatography using CH_2Cl_2/CH_3OH (v/v, 50:1) as the eluent. This resulted in the final product, compound **2**, which was a white solid (0.32 g, 85% yield). ^{1}H NMR (500 MHz, Methanol-d_4) δ 7.57−7.49 (m, 2H), 7.34−7.25 (m, 2H), 4.56 (d, J = 6.2 Hz, 3H), 4.02−3.82 (m, 2H), 3.73−3.55 (m, 2H), 2.31−1.92 (m, 4H), 1.43 (s, 9H); HR-MS (ESI, m/z): $[M + Na]^+$ calcd for $C_{19}H_{27}N_3NaO_5^+$ 400.1843, found 400.1830 (Figures S1 and S2).

Synthesis of MB-Boc. Compound **2** (150 mg, 0.4 mmol) and pyridine (2.0 mL) were added to a solution of compound **1** under a nitrogen atmosphere. After DMAP (120 mg, 1.0 mmol) was added, the mixture was reacted at 45 °C overnight. The progress of the reaction was monitored by TLC until completion. After the reaction was complete, the solvent was

https://doi.org/10.1021/acs.analchem.3c02909
Anal. Chem. 2023, 95, 17577−17585

removed under reduced pressure and the crude product was washed with ether. The supernatant was collected and evaporated, leaving a solid substance that was subsequently extracted three times with CH_2Cl_2 and 1 M HCl. The organic layer was dried over Na_2SO_4 and then filtered, and the resulting residue was vacuum-dried. The product was finally purified by silica gel column chromatography using CH_2Cl_2/CH_3OH (v/v, 10:1) as the eluent, yielding the blue solid product MB-Boc (0.22 g, 33% yield). ^{1}H NMR (300 MHz, Chloroform-*d*) δ 9.38 (s, 1H), 7.49 (d, J = 8.3 Hz, 2H), 7.34 (d, J = 8.5 Hz, 2H), 7.22 (d, J = 8.3 Hz, 2H), 6.76 (d, J = 13.2 Hz, 4H), 5.43 (s, 1H), 5.13 (s, 2H), 4.73 (d, J = 8.0 Hz, 1H), 4.07−3.85 (m, 2H), 3.56 (t, J = 9.3 Hz, 1H), 3.41 (q, J = 9.7, 8.8 Hz, 1H), 2.93 (s, 12H), 2.28−1.83 (m, 4H), 1.44 (s, 9H); ^{13}C NMR (126 MHz, $CDCl_3$) δ 169.51, 168.63, 155.90, 154.41, 148.71, 137.87, 132.78, 132.04, 128.63, 128.31, 127.00, 119.70, 111.17, 110.42, 79.99, 67.34, 61.02, 46.55, 43.16, 40.77, 28.36, 26.96, 24.96. HR-MS (ESI, m/z): $[M + H]^+$ calcd for $C_{36}H_{45}N_6O_6S^+$ 689.3116, found 689.3134; $[M + Na]^+$ calcd for $C_{36}H_{44}N_6NaO_6S^+$ 711.2935, found 711.2959; $[M+K]^+$ calcd for $C_{36}H_{44}N_6KO_6S^+$ 727.2675, found 727.2745 (Figures S3−S5).

Synthesis of MB-DPP4. MB-Boc (69 mg, 0.11 mmol) was dissolved in CH_2Cl_2 (4 mL). Trifluoroacetic acid (4 mL) was then introduced into the solution, and the mixture was stirred at room temperature for 1 h. The reaction's progress was monitored by TLC until completion. Following the reaction, the solvent was removed under reduced pressure. The resultant compound was subsequently purified by silica gel chromatography using CH_2Cl_2/CH_3OH (v/v, 10:1) as the eluent, yielding MB-DPP4 as a light blue solid (63.48 mg, 83% yield). ^{1}H NMR (300 MHz, DMSO-d_6) δ 10.19 (s, 1H), 7.57 (d, J = 8.5 Hz, 2H), 7.33−7.23 (m, 4H), 6.75−6.58 (m, 4H), 5.09 (s, 2H), 4.53−4.42 (m, 1H), 3.72 (s, 1H), 3.61−3.48 (m, 3H), 2.88 (s, 12H), 2.19−1.89 (m, 4H); ^{13}C NMR (126 MHz, Methanol-d_4) δ 170.98, 164.87, 154.84, 148.79, 137.93, 132.82, 132.16, 128.22, 128.10, 126.76, 119.91, 111.00, 110.05, 67.17, 61.01, 46.33, 40.11, 39.61, 29.48, 24.25; HR-MS (ESI, m/z): $[M]^+$ calcd for $C_{23}H_{22}NO_2^+$ 588.2519, found 588.2512 (Figures S6−S8).

General Procedure for DPP-IV Detection. A 1 mM stock solution of probe MB-DPP4 was prepared by dissolving MB-DPP4 in a DMSO solvent. The reaction system with a total volume of 300 μL consisted of enzyme/serum/urine, phosphate-buffered saline (PBS), and the probe (containing 1% DMSO). To assemble the reaction, 3 μL of MB-DPP4 was added to 200 μL of phosphate buffer (PBS, pH 7.4, 10 mM) in a 2 mL centrifuge tube. This was followed by the addition of a DPP-IV solution at varying concentrations; after that, the volume was adjusted to 300 μL using PBS. A control solution, which was absent from DPP-IV, was also prepared and measured under identical conditions. The reaction mixture was then incubated for 1.5 h at 37 °C in a constant-temperature shaker incubator to stimulate the enzymatic digestion process. Upon completion of the reaction, the mixture was transferred to a 1 cm quartz cuvette for UV−vis absorption and fluorescence measurements under the following settings: excitation and emission slit widths = 2.5 nm, λ_{ex} = 665 nm, and PMT = 700 V.

Establishment of the Mouse Model. All animal experiments were conducted in accordance with the ethical guidelines established by the Institutional Animal Care and Use Committee (IACUC) of Jilin University (animal experimental ethical inspection permit number: SY202306031). Female NOD/SCID mice (6−8 weeks old) were used for *in vivo* imaging of exogenous DPP-IV. A TPC-1 cell suspension (containing approximately 1 × 10^6 cells dissolved in 50 μL of PBS) was subcutaneously injected into the back of mice, and the tumors were allowed to grow for approximately 3 weeks.

We performed three groups of fluorescence imaging experiments. In the control group, a mouse was intratumorally injected with MB-DPP4 (200 μM, 50 μL). In the second group, the probe MB-DPP4 (200 μM, 50 μL) was injected into the same site of a tumor-bearing mouse. Mice in both groups were subjected to fluorescence imaging 1 h after injection. In the third group, a mouse was dissected, and its organs including the heart, liver, spleen, lung, and kidney as well as its TPC-1 tumor were removed. These samples were then incubated with MB-DPP4 (200 μM) for 1 h before fluorescence imaging.

Mice were anesthetized with isoflurane before being subjected to *in vivo* imaging experiments, which were performed using an IVIS Lumina LT Series III small animal imaging system at an excitation wavelength of 665 nm.

RESULTS AND DISCUSSION

Design and Mechanism of MB-DPP4. Currently, a significant shortfall of fluorescent probes for DPP-IV detection lies in their effectiveness as many of these probes exhibit high background fluorescence signals. Methylene blue (MB) and its derivatives, which are categorized as near-infrared dyes, possess a remarkably robust structure. The well π-conjugated phenothiazine ring, which is intrinsic to the MB structure, can be dismantled as a result of reduction by sodium dithionite, leading to the generation of two benzene ring structures devoid of π-conjugation. This structural alteration makes these dyes excellent candidates for the fabrication of fluorescent probes with reduced background signals. The design process of enzyme-activated fluorescent probes leads to formidable challenges, encompassing not only the choice of fluorophore and the specificity of the recognition group but also the overall probe architecture. Certain enzyme substrates contain narrow channels that could hinder the fluorescent probe from accessing its active site, thereby suppressing enzyme-triggered probe activation. To surmount this constraint, we engineered the MB-DPP4 probe. This innovative probe was incorporated with a linker group—specifically, 4-aminobenzyl alcohol—strategically positioned between the recognition group and the fluorophore.

The integration of this linker group fulfills several objectives: (i) Extending the separation between the recognition group and the fluorophore; (ii) mitigating the steric hindrance enveloping the recognition group; (iii) facilitating the probe's recognition group in accessing deeper areas of the enzyme's active site. As a result, the probability of enzymatic reactions is amplified, allowing for an enhanced detection sensitivity. The recognition mechanism of the fluorescent probe MB-DPP4 is illustrated in Figure 1A. The modification of the phenothiazine fluorophore with glycine-L-proline as the recognition group, via a cleavable linker, locks the resulting probe in a non-π-conjugated, colorless, and nonfluorescent state. However, in the presence of DPP-IV, the glycine-L-proline moiety is specifically hydrolyzed followed by 1,6-elimination in a domino decomposition, which leads to the restoration of the large π-conjugation and strong near-infrared fluorescence of MB.

https://doi.org/10.1021/acs.analchem.3c02909
Anal. Chem. 2023, 95, 17577−17585

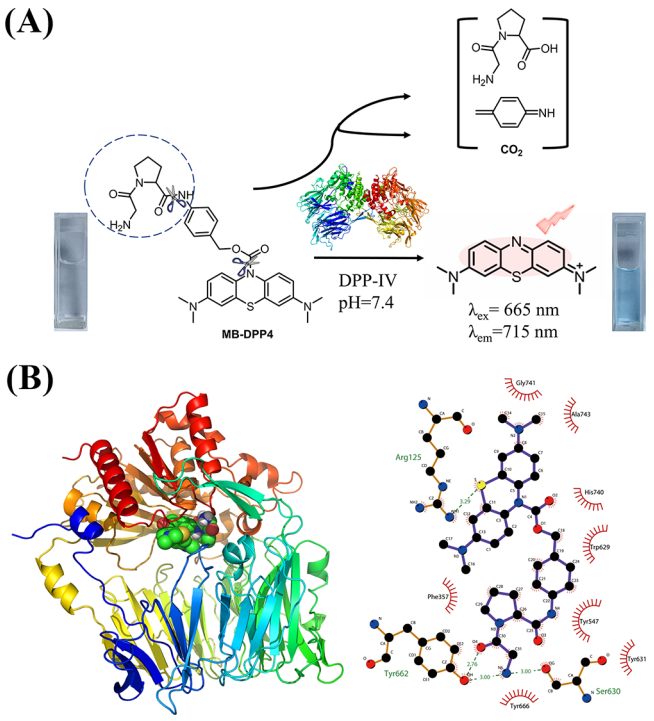

Figure 1. (A) Structure of MB-DPP4 and its reaction with DPP-IV. (B) Simulation of interactions between MB-DPP4 and DPP-IV.

The binding of MB-DPP4 to DPP-IV was investigated using molecular docking.[36] As depicted in Figure 1B, MB-DPP4 readily enters the active site of DPP-IV, forming four hydrogen bonds with three amino acids: ARG-125, SER-630, and TYR-662. A binding energy of −8.7 kcal/mol suggests that the probe MB-DPP4 has a strong binding affinity toward DPP-IV.

To further validate that MB-DPP4 was hydrolyzed, we examined the reaction product using LC-MS. Upon activation by DPP-IV, the mass peak of MB-DPP4 shifted from m/z 588.1784 to m/z 283.8850 (Figure S9), which aligns with the mass peak of MB (m/z 283.9009) (Figure S10). The retention times for MB-DPP4 and MB were 3.07 and 3.37 min, respectively. When the probe was incubated with DPP-IV, a new peak with gradually increasing height emerged at t = 3.37 min, which is consistent with the retention time of the product MB (Figure S11). These findings indicate that DPP-IV can cleave the glycine-L-proline substrate in the probe, thereby restoring the conjugated and fluorescent structure.

Spectral Properties of MB-DPP4 and Optimization of Reaction Conditions. This investigation was conducted to study the fluorescence and UV−vis absorption spectral properties of MB-DPP4 under a DPP-IV titration. As depicted in Figure 2A, MB-DPP4 did not exhibit a noticeable absorption peak in the visible region due to the absence of a large internal conjugated structure. However, upon the addition of DPP-IV, a new absorption peak emerged at 665 nm, which aligns with the maximum absorption wavelength of the fluorophore MB. The color of the system transitioned from colorless to blue, which was observable with the naked eye. At an excitation wavelength of 665 nm, MB-DPP4 exhibited minimal fluorescence. However, following the addition of DPP-IV, the fluorescence intensity at 715 nm sharply increased, nearly coinciding with the fluorescence peak of the fluorophore MB (Figure 2B). These results further confirm that MB-DPP4 reacts with DPP-IV to produce the fluorophore MB.

The response of MB-DPP4 to DPP-IV under various reaction conditions, including reaction time, pH values, and temperatures, was examined. In the absence of DPP-IV, the probe did not emit any fluorescence and the fluorescence intensity remained essentially stable over time. This indicates that MB-DPP4 was stable under physiological buffer conditions. Upon the addition of DPP-IV at varying concentrations, the fluorescence signal of the probe gradually increased, reaching saturation at 1.5 h (Figure S12A). Consequently, the reaction time was set to 1.5 h. The fluorescence intensity of MB-DPP4 was low at a pH range of 3−9, but upon the introduction of DPP-IV, the probe exhibited an intense fluorescence signal at pH 7.4 (Figure S12B). In subsequent *in vivo* biological studies, pH 7.4 was selected as the optimal pH condition. As shown in Figure S12C, upon the addition of 0.2 μg/mL DPP-IV, the fluorescence intensity of the probe gradually increased with increasing temperature. Therefore, the physiological temperature, 37 °C, was selected for subsequent experiments. Furthermore, photobleaching can irreversibly affect a probe when it is applied in applications such as cellular imaging. Fortunately, the fluorescence intensity of the probe MB-DPP4 and the reaction system remained essentially unaffected after being continuously irradiated with a xenon lamp for 1 h, which

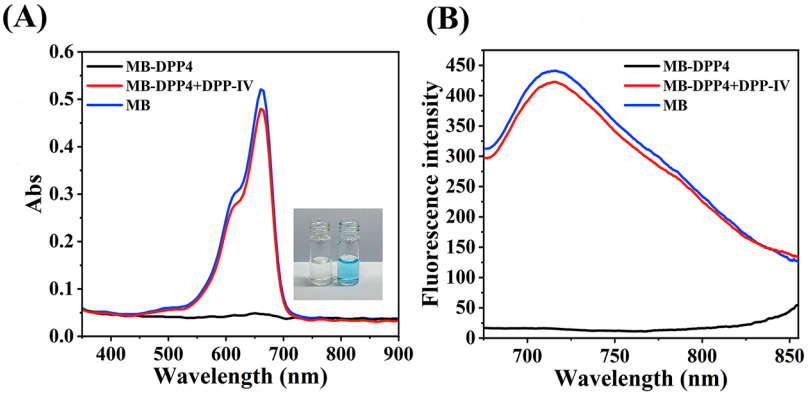

Figure 2. (A) UV−vis absorption and (B) fluorescence spectra of MB-DPP4 (10 μM), MB-DPP4 in the presence of DPP-IV (2 μg/mL), and MB (10 μM) in PBS (10 mM, pH 7.4) measured at 37 °C over a duration of 1.5 h. The measurement was conducted at excitation and emission wavelengths of 665 and 715 nm, respectively. The inset illustrates the color and fluorescence changes of the solution under natural daylight.

https://doi.org/10.1021/acs.analchem.3c02909
Anal. Chem. 2023, 95, 17577−17585

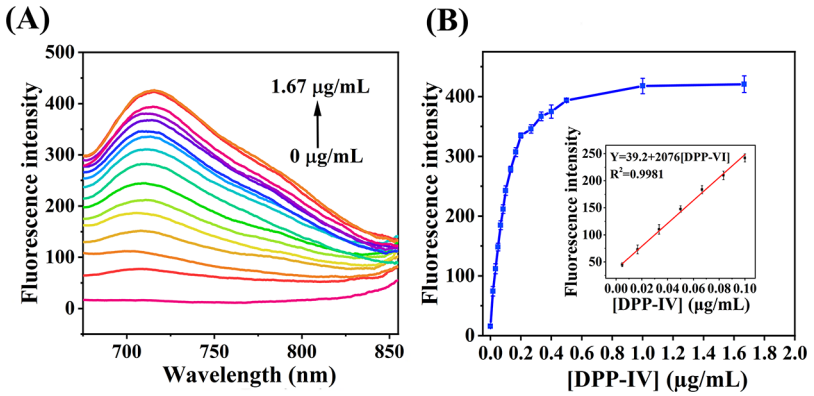

Figure 3. (A) Fluorescence spectra of MB-DPP4 (10 μM) following the addition of varying concentrations of DPP-IV (0−1.67 μg/mL). (B) Linear relationship between the fluorescence intensity and DPP-IV concentration. Data are presented as the mean ± SD (n = 3). The measurement was conducted at excitation and emission wavelengths of 665 and 715 nm, respectively.

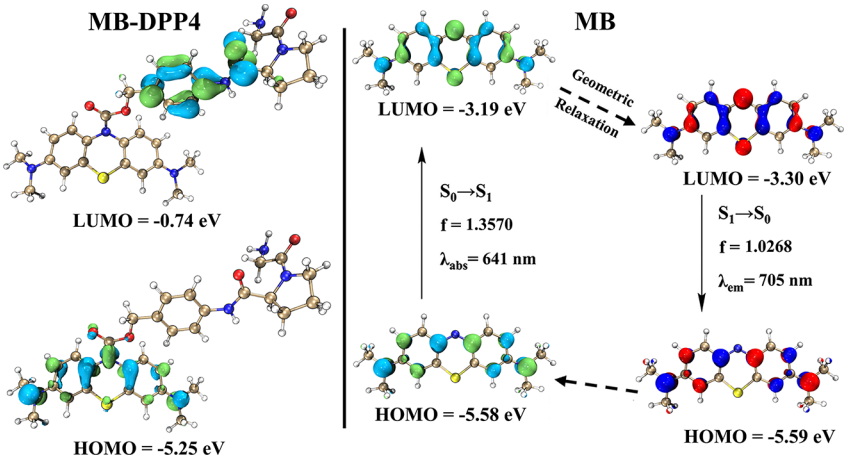

Figure 4. Vertical excitation energy, oscillator strength (f), wavelength, and relevant frontier molecular orbits for primary absorption and emission of MB-DPP4 and MB. The two molecules were modeled at their TDDFT levels based on the optimal structures at the ground and first excited states.

indicates that MB-DPP4 possesses excellent photostability (Figure S12D). These results suggest that the sensing system has robust optical stability. Therefore, *in vitro* experiments were conducted at 37 °C and pH 7.4 to simulate the physiological conditions of biological systems.

Standard Curve and Detection Limit of DPP-IV. A study of the dependency of enzymatic reaction on concentration was conducted under optimal experimental conditions. As illustrated in Figure 3A, the fluorescence intensity at 715 nm increased (by 40-fold) with rising DPP-IV concentration. Notably, a strong linear relationship was observed between the fluorescence intensity and the DPP-IV concentration in the range of 0.005−0.10 μg/mL (Figure 3B). Furthermore, MB-DPP4 was capable of detecting DPP-IV at low concentrations with a detection limit of 0.29 ng/mL (3 S/N, n = 11). Compared to previously reported DPP-IV-specific fluorescent probes,[19,31,32,34,35,37,38] MB-DPP4 had superior sensitivity and better sensing performance (Table S1).

Reaction Kinetics. The kinetic interactions between MB-DPP4 and DPP-IV were rigorously investigated. As illustrated in the Michaelis−Menten plot (Figure S13A), there was a marked escalation in the initial reaction rates corresponding to the increasing concentrations of MB-DPP4, ranging from 1 to 100 μM. Subsequent analysis via the Lineweaver−Burk plot (Figure S13B) revealed a maximal velocity (V_{max}) of 0.309 μM/min, along with a Michaelis constant (K_m) of 13.38 μM. Notably, this K_m value is significantly lower than that of the conventional substrate Gly-Pro-pNA (K_m = 265.5 μM),[39] highlighting the exceptional affinity and sensitivity of MB-DPP4 toward DPP-IV.

Selectivity. The selectivity of MB-DPP4 was evaluated by using a series of potential interferents such as different cations, anions, amino acids, sera, proteins, and enzymes. As anticipated, only DPP-IV led to a significant enhancement in fluorescence; other interferents had a minimal effect on the fluorescence signal. A mixture of DPP-IV with vildagliptin and MB-DPP4 led to the inhibition of the fluorescence signal. This observation confirms that MB-DPP4 has high selectivity toward DPP-IV and is suitable for detecting DPP-IV in complex biological systems without being affected by interference from other substances (Figure S14).

Theoretical Calculations. To elucidate the changes in the molecular spectra of MB-DPP4 and MB pre- and postreaction, theoretical calculations were performed to examine their ground state geometries and electronic structures (Figure 4). MB-DPP4 did not exhibit significant visible absorption and emission due to the lack of substantial intramolecular conjugated structure; as a result, a clear separation of the HOMO-LUMO electron clouds was observed. Upon incubating with DPP-IV, MB-DPP4 was transformed into MB,

https://doi.org/10.1021/acs.analchem.3c02909
Anal. Chem. 2023, 95, 17577−17585

forming large π-bonds within the molecule; as a result, the HOMO-LUMO electron clouds were observed to concentrate primarily in the phenoxazine structure. The absorption and emission spectra were calculated by TDDFT. Both the $S_0 \rightarrow S_1$ and $S_1 \rightarrow S_0$ transitions of MB occurred between the HOMO and LOMO orbitals with energy gaps of 2.39 and 2.29 eV, respectively, which correspond to a maximum absorption peak of 641 nm ($f = 1.3570$) and a fluorescence peak of 705 nm ($f = 1.0268$). These results show that the theoretical calculations are in complete agreement with the experimental spectral results.

Determination of DPP-IV in Human Serum and Urine. The levels of DPP-IV in biological samples (human serum, urine, etc.) are crucial indicators for the evaluation and early diagnosis of thyroid diseases.[40−42] Determined by our method, the recovery of DPP-IV in spiked human serum samples ranged from 96.5 to 102.2% (Table 1). These high recovery rates indicate that MB-DPP4 can accurately detect DPP-IV in actual serum samples. Furthermore, the reliability of the developed probe in detecting DPP-IV was assessed. The probe was employed to detect DPP-IV spiked at different amounts in human urine samples, from which the recovery rates were found to range from 98.3 to 103.5% (Table 2). The concentrations of DPP-IV in serum and urine samples were found to be 43.42 and 3.64 ng/mL, respectively. The findings show that our detection methods are comparable to commercial ELISA kits, suggesting that the developed MB-DPP4 could serve as a powerful tool for the precise and efficient detection of DPP-IV in biological samples such as human serum and urine.

Table 1. Recovery Rates of DPP-IV Spiked into Diluted Human Serum ($n = 3$)

DPP-IV added (ng/mL)	DPP-IV found by our method (ng/mL)[a]	recovery (%)	DPP-IV found by ELISA (ng/mL)[a]
0	43.42 ± 1.65		42.61 ± 1.02
40	83.22 ± 1.33	99.5	82.49 ± 1.35
60	101.32 ± 1.01	96.5	99.67 ± 1.47
80	125.18 ± 0.97	102.2	123.82 ± 0.93

[a]Mean of three determinations ± standard deviation.

Table 2. Recovery Rates of DPP-IV Spiked into Diluted Human Urine ($n = 3$)

DPP-IV added (ng/mL)	DPP-IV found by our method (ng/mL)[a]	Recovery (%)	DPP-IV found by ELISA (ng/mL)[a]
0	3.64 ± 0.03		3.61 ± 0.02
4	7.57 ± 0.05	98.3	7.48 ± 0.01
8	11.69 ± 0.09	100.6	11.42 ± 0.03
12	16.06 ± 0.12	103.5	14.79 ± 0.05

[a]Mean of three determinations ± standard deviation.

Cytotoxicity Experiments. Cytotoxicity experiments were carried out to evaluate the safety and biocompatibility of MB-DPP4. Prior to cell imaging, the cytotoxicity of MB-DPP4 with doses ranging from 0 to 50 μM was assessed using the CCK-8 test (Figure S15). The results showed that the survival rate of TPC-1 cells was >80% after 48 h of exposure to MB-DPP4, which confirms the low cytotoxicity of MB-DPP4. Additionally, the hemolysis assay was used to further validate the biocompatibility of MB-DPP4. The results showed that the hemolysis rate of MB-DPP4 at concentrations below 200 μM was only 2%, which is indicative of its high biocompatibility and in turn high suitability for cell imaging (Figure S16).

Probing Endogenous DPP-IV Activity in Cells. Given the preliminary results, the potential of MB-DPP4 as a probe for detecting endogenous DPP-IV in live cells was further evaluated (Figure 5). Both cell types in the control groups yielded weak, essentially negligible background fluorescence. Control experiments yielded weak, essentially negligible background fluorescence for both cell types (Figure 5a,d). We imaged both normal (Nthy-ori3-1) and cancerous (TPC-1) cells after incubation with MB-DPP4. A markedly bright fluorescence was observed in TPC-1 cells (Figure 5e), while only faint fluorescence was detected in Nthy-ori3-1 cells (Figure 5b). These observations suggest an overexpression of DPP-IV in thyroid cancer cells, which aligns with the literature.

To ensure that the fluorescence observed originated from endogenous DPP-IV, we conducted inhibitor and inducer experiments. TPC-1 cells pretreated with vildagliptin and subsequently incubated with MB-DPP4 did not exhibit significant fluorescence (Figure 5f). Conversely, cells pretreated with genistein exhibited enhanced fluorescence compared to cells incubated with the control probe (Figure 5c,g). These data suggest that the fluorescence variations are caused by the endogenous DPP-IV activity. Therefore, MB-DPP4 may serve as a molecular tool for detecting DPP-IV activity and distinguishing between normal and cancerous cells in thyroid tissues.

Furthermore, we established a coculture model (Nthy-ori3-1 and TPC-1 cells) to simulate the tumor microenvironment *in vivo*. As illustrated in Figure S17, Nthy-ori3-1 cells stained with Hoechst33342 displayed significant fluorescence in the blue channel with minimal fluorescence in the red channel. Conversely, the unstained nuclei of thyroid cancer cells exhibited a stronger red fluorescence, indicating that MB-DPP4 can effectively monitor DPP-IV variations and distinguish between normal and cancerous cells.

***In Vivo* Imaging Experiments in Mice.** To further validate the practical applicability of MB-DPP4, *in vivo* imaging experiments were conducted. A human thyroid-tumor-bearing mouse model was established using NOD/SCID mice. We observed that the fluorescence intensity of the tumor-bearing group significantly exceeded that of the control group, which suggests an elevated level of DPP-IV in the thyroid tumor mice (Figure 6A). A time-course experiment further revealed that the fluorescence could be detected in the tumor as early as 15 min postinjection with the intensity gradually increasing over time. The fluorescence reached a plateau at 60 min, as shown in Figure S18. Subsequent imaging, as shown in Figure 6B, revealed distinct contrasts between the dissected organs and tumor. With identical imaging settings, the fluorescence signal of the tumors was distinctly observable, while that of the heart/lung, liver, spleen, and kidney was indiscernible. These findings suggest that MB-DPP4 is a promising tool for *in vivo* imaging studies of DPP-IV and could potentially contribute to the early clinical detection of thyroid conditions. With superior detection capability, MB-DPP4 offers an innovative approach for the preliminary diagnosis and evaluation of thyroid cancer.

CONCLUSIONS

In conclusion, a highly sensitive and selective enzyme-activated NIR fluorescent probe, MB-DPP4, was developed for the

https://doi.org/10.1021/acs.analchem.3c02909
Anal. Chem. 2023, 95, 17577−17585

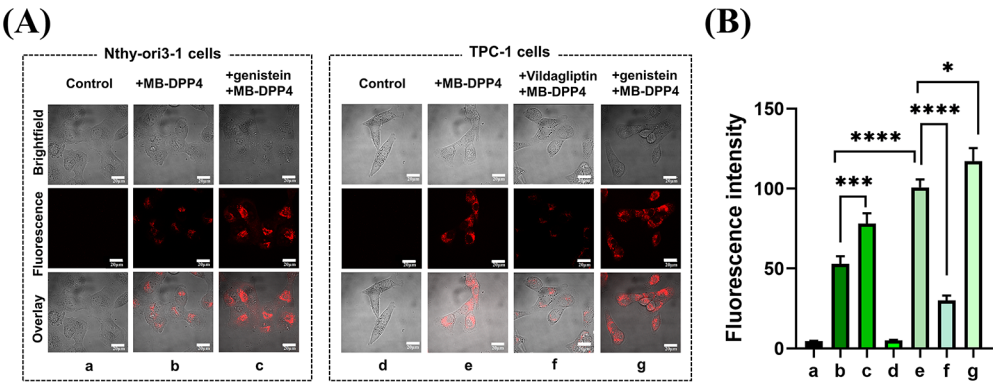

Figure 5. (A) Fluorescence images depicting endogenous MB-DPP4 in Nthy-ori3-1 and TPC-1 cells: (a) untreated Nthy-ori3-1 cells; (b) Nthy-ori3-1 cells incubated with MB-DPP4 (10 μM) for 1 h; (c) Nthy-ori3-1 cells treated with genistein (20 μg/mL) for 24 h followed by MB-DPP4 for 1 h; (d) untreated TPC-1 cells; (e) TPC-1 cells incubated with MB-DPP4 (10 μM) for 1 h; (f) TPC-1 cells treated with vildagliptin (50 μM) for 1 h followed by MB-DPP4 for another 1 h; (g) TPC-1 cells treated with genistein (20 μg/mL) for 24 h followed by MB-DPP4 for 1 h. Scale bars: 20 μm. (B) Fluorescence intensity of (a−g) in panel (A). From top to bottom: brightfield, fluorescence, and overlay images (****P < 0.0001, all data analyses were conducted using an independent sample t-test, assuming that the variances are equal, means ± SD, n = 7. λ_{ex} = 665 nm, λ_{em} = 700−730 nm).

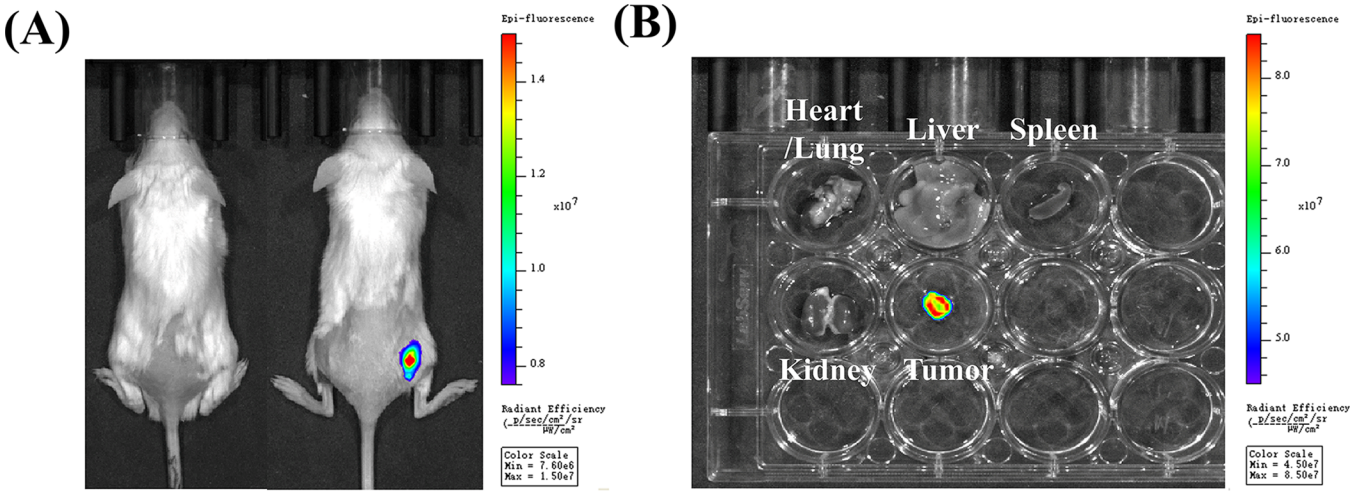

Figure 6. (A) Fluorescence images displaying DPP-IV activity in a normal mouse (left) and thyroid tumor mouse (right) captured following intratumoral injection of MB-DPP4 (200 μM, 50 μL). (B) Fluorescence images showcasing the primary internal organs and the thyroid tumor of mice.

specific detection of DPP-IV. MB-DPP4 exhibited a low background fluorescence signal and had a maximum emission wavelength of 715 nm. It led to remarkably high fluorescence enhancement and had a low DPP-IV detection limit of 0.29 ng/mL. Biological assays indicated that MB-DPP4 possessed excellent biocompatibility, and with its ability to detect endogenous DPP-IV, it could discern between normal thyroid cells and thyroid cancer cells. Moreover, it could detect the overexpression of DPP-IV in a thyroid-cancer-bearing mouse model, which marks this work as the first study on DPP-IV expression levels in thyroid disease using fluorescent probes. This study establishes a paradigm for the design of next-generation probes with low background signals as it not only bolsters the understanding of biological processes and enhances analyte-monitoring capabilities but also introduces an innovative way for fabricating a high-performance molecular tool for the early diagnosis of thyroid diseases and screening of therapeutic drugs.

■ ASSOCIATED CONTENT

Supporting Information

The Supporting Information is available free of charge at https://pubs.acs.org/doi/10.1021/acs.analchem.3c02909.

Additional experimental details, including materials and instruments, determination of the detection limit, enzymatic kinetics assays, theoretical calculation and analysis, molecular docking, CCK-8 assay, cell culture and imaging, hemolysis assay, and supplementary figures and table (PDF)

■ AUTHOR INFORMATION

Corresponding Authors

Pinyi Ma − *College of Chemistry, Jilin Province Research Center for Engineering and Technology of Spectral Analytical Instruments, Jilin University, Changchun 130012, China;* orcid.org/0000-0002-3230-4928; Email: mapinyi@jlu.edu.cn

Qiang Fei − *College of Chemistry, Jilin Province Research Center for Engineering and Technology of Spectral Analytical*

Instruments, Jilin University, Changchun 130012, China; orcid.org/0000-0001-8757-2914; Email: feiqiang@jlu.edu.cn

Authors

Jiaxin Li − *College of Chemistry, Jilin Province Research Center for Engineering and Technology of Spectral Analytical Instruments, Jilin University, Changchun 130012, China*

Mo Ma − *College of Chemistry, Jilin Province Research Center for Engineering and Technology of Spectral Analytical Instruments and School of Pharmacy, Jilin University, Changchun 130012, China*

Jingkang Li − *College of Chemistry, Jilin Province Research Center for Engineering and Technology of Spectral Analytical Instruments, Jilin University, Changchun 130012, China*

Lanlan Xu − *College of Chemistry, Jilin Province Research Center for Engineering and Technology of Spectral Analytical Instruments, Jilin University, Changchun 130012, China*

Daqian Song − *College of Chemistry, Jilin Province Research Center for Engineering and Technology of Spectral Analytical Instruments, Jilin University, Changchun 130012, China;* orcid.org/0000-0002-4866-1292

Complete contact information is available at: https://pubs.acs.org/10.1021/acs.analchem.3c02909

Notes

The authors declare no competing financial interest.

■ ACKNOWLEDGMENTS

This work was supported by the National Natural Science Foundation of China (22004046 and 22074052) and the Science and Technology Developing Foundation of Jilin Province of China (nos. 20230101033JC, 20230204116YY, and YDZJ202302CXJD031).

■ REFERENCES

(1) Li, J.; Cao, J.; Wu, W.; Xu, L.; Zhang, S.; Ma, P.; Wu, Q.; Song, D. *Sensors and Actuators B-Chemical* **2023**, *377*, No. 133122.
(2) Cuesta, S. M.; Rahman, S. A.; Furnham, N.; Thornton, J. M. *Biophys. J.* **2015**, *109*, 1082−1086.
(3) Yu, D. M. T.; Yao, T.-W.; Chowdhury, S.; Nadvi, N. A.; Osborne, B.; Church, W. B.; McCaughan, G. W.; Gorrell, M. D. *Febs Journal* **2010**, *277*, 1126−1144.
(4) Mulvihill, E. E.; Drucker, D. J. *Endocrine Reviews* **2014**, *35*, 992−1019.
(5) Raj, V. S.; Mou, H.; Smits, S. L.; Dekkers, D. H. W.; Mueller, M. A.; Dijkman, R.; Muth, D.; Demmers, J. A. A.; Zaki, A.; Fouchier, R. A. M.; Thiel, V.; Drosten, C.; Rottier, P. J. M.; Osterhaus, A. D. M. E.; Bosch, B. J.; Haagmans, B. L. *Nature* **2013**, *495*, 251−254.
(6) Kluess, H. A. *Front. Physiol.* **2020**, *11*, 148.
(7) Kreymann, B.; Williams, G.; Ghatei, M. A.; Bloom, S. R. *Lancet* **1987**, *330*, 1300−1304.
(8) Drucker, D. J.; Nauck, M. A. *Lancet* **2006**, *368*, 1696−1705.
(9) Tahrani, A. A.; Barnett, A. H.; Bailey, C. J. *Nature Reviews Endocrinology* **2016**, *12*, 566−592.
(10) Beckenkamp, A.; Davies, S.; Willig, J. B.; Buffon, A. *Tumor Biology* **2016**, *37*, 7059−7073.
(11) Sánchez-Otero, N.; Rodríguez-Berrocal, F. J.; de la Cadena, M. P.; Botana-Rial, M. I.; Cordero, O. J. *Sci. Rep.* **2014**, *4*, 3999.
(12) Perner, F.; Gyuris, T.; Rakoczy, G.; Sarvary, E.; Gorog, D.; Szalay, F.; Kunos, I.; Szonyi, L.; Peterfy, M.; Takacs, L. *Journal of Laboratory and Clinical Medicine* **1999**, *134*, 56−67.
(13) Barchetta, I.; Ceccarelli, V.; Cimini, F. A.; Barone, E.; Sentinelli, F.; Coluzzi, M.; Chiappetta, C.; Bertoccini, L.; Tramutola, A.; Labbadia, G.; Di Cristofano, C.; Silecchia, G.; Leonetti, F.; Cavallo, M. G. *Journal of Endocrinological Investigation* **2021**, *44*, 979−988.
(14) La Vecchia, C.; Malvezzi, M.; Bosetti, C.; Garavello, W.; Bertuccio, P.; Levi, F.; Negri, E. *Int. J. Cancer* **2015**, *136*, 2187−2195.
(15) Gonzalez-Gonzalez, R.; Bologna-Molina, R.; Carreon-Burciaga, R. G.; Gómezpalacio-Gastelum, M.; Molina-Frechero, N.; Salazar-Rodríguez, S. *ISRN Oncol.* **2011**, *2011*, No. 915925.
(16) Abicic, I.; Prpic, T.; Bogovic, V.; Milankovic, S. G.; Mihalj, H.; Vceva, A.; Zubcic, Z.; Sestak, A.; Rezo, M. *Acta Clin. Croat.* **2020**, *59*, 108−114.
(17) Tanaka, T.; Umeki, K.; Yamamoto, I.; Sakamoto, F.; Noguchi, S.; Ohtaki, S. *Int. J. Cancer* **1995**, *64*, 326−331.
(18) Larrinaga, G.; Blanco, L.; Errarte, P.; Beitia, M.; Sanz, B.; Perez, I.; Irazusta, A.; Sánchez, C. E.; Santaolalla, F.; Andrés, L.; López, J. I. *Dis. Markers* **2013**, *35*, 825−832.
(19) Valverde-Pozo, J.; Paredes, J. M.; Widmann, T. J.; Griñan-Lison, C.; Ceccarelli, G.; Gioiello, A.; Garcia-Rubiño, M. E.; Marchal, J. A.; Alvarez-Pez, J. M.; Talavera, E. M. *ACS Sens.* **2023**, *8*, 1064−1075.
(20) Aratake, Y.; Kotani, T.; Tamura, K.; Araki, Y.; Kuribayashi, T.; Konoe, K.; Ohtaki, S. *American Journal of Clinical Pathology* **1991**, *96*, 306−310.
(21) Bartolazzi, A.; Gasbarri, A.; Papotti, M.; Bussolati, G.; Lucante, T.; Khan, A.; Inohara, H.; Marandino, F.; Orlandi, F.; Nardi, F.; Vecchione, A.; Tecce, R.; Larsson, O. *Lancet* **2001**, *357*, 1644−1650.
(22) Jeong, S. H.; Hong, H. S.; Lee, E. H. *Ultrasound Quarterly* **2016**, *32*, 349−355.
(23) Hino, R.; Inoshita, N.; Yoshimoto, T.; Ogawa, M.; Miura, D.; Watanabe, R.; Watanabe, K.; Kamiya, M.; Urano, Y. *Thyroid Res.* **2018**, *11*, 16.
(24) Lei, Z.; Li, X.; Luo, X.; He, H.; Zheng, J.; Qian, X.; Yang, Y. *Angew. Chem., Int. Ed.* **2017**, *56*, 2979−2983.
(25) Sun, B.; Hettie, K. S.; Zhu, S. *Adv. Ther.* **2021**, *4*, 2000278.
(26) Chen, H.; Dong, B.; Tang, Y.; Lin, W. *Acc. Chem. Res.* **2017**, *50*, 1410−1422.
(27) Xu, L.; Ma, M.; Li, J.; Gao, D.; Ma, P.; Zhang, F.; Song, D. *Anal. Chem.* **2023**, *95*, 12089−12096.
(28) Xu, L.; Chu, H.; Gao, D.; Wu, Q.; Sun, Y.; Wang, Z.; Ma, P.; Song, D. *Anal. Chem.* **2023**, *95*, 2949−2957.
(29) Li, M.; Ma, H.; Shi, C.; Zhang, H.; Long, S.; Sun, W.; Du, J.; Fan, J.; Peng, X. *Chemical Research in Chinese Universities* **2021**, *37*, 925−933.
(30) Cordero, O. J.; Salgado, F. J.; Nogueira, M. *Cancer Immunol., Immunother.* **2009**, *58*, 1725−1749.
(31) Wang, J.; Zhang, L.; Qin, W.; Liu, Y. *Anal. Chim. Acta* **2022**, *1221*, No. 340147.
(32) Wang, J.; Zhang, L.; Qu, Y.; Yang, Y.; Cao, T.; Cao, Y.; Iqbal, A.; Qin, W.; Liu, Y. *Anal. Chem.* **2021**, *93*, 11461−11469.
(33) Guo, X.; Mu, S.; Li, J.; Zhang, Y.; Liu, X.; Zhang, H.; Gao, H. *J. Mater. Chem. B* **2020**, *8*, 767−775.
(34) Zou, L.-W.; Wang, P.; Qian, X.-K.; Feng, L.; Yu, Y.; Wang, D.-D.; Jin, Q.; Hou, J.; Liu, Z.-H.; Ge, G.-B.; Yang, L. *Biosens. Bioelectron.* **2017**, *90*, 283−289.
(35) Gong, Q.; Shi, W.; Li, L.; Wu, X.; Ma, H. *Anal. Chem.* **2016**, *88*, 8309−8314.
(36) Song, L.; Sun, M.; Shi, J.; Tian, Z.; Song, Y.; Liu, H.; Zhao, S.; Yin, H.; Ge, G. *Anal. Chem.* **2023**, *95*, 5489−5493.
(37) Xing, J.; Gong, Q.; Zhang, R.; Sun, S.; Zou, R.; Wu, A. *Chem. Commun.* **2018**, *54*, 8773−8776.
(38) Liu, T.; Ning, J.; Wang, B.; Dong, B.; Li, S.; Tian, X.; Yu, Z.; Peng, Y.; Wang, C.; Zhao, X.; Huo, X.; Sun, C.; Cui, J.; Feng, L.; Ma, X. *Anal. Chem.* **2018**, *90*, 3965−3973.
(39) Liu, J.; Cheng, X.; Fu, L. *Analytical Methods* **2012**, *4*, 1797−1805.
(40) Firneisz, G.; Varga, T.; Lengyel, G.; Feher, J.; Ghyczy, D.; Wichmann, B.; Selmeci, L.; Tulassay, Z.; Racz, K.; Somogyi, A. *PLoS One* **2010**, *5*, No. e12226.
(41) Zhang, Y.; Fu, Y.; Yang, Y.; Ke, J.; Zhao, D. *J. Int. Med. Res.* **2022**, *50*, No. 030006052211120.

(42) Zhang, J.; Qian, X.-K.; Song, P.-F.; Li, X.-D.; Wang, A.-Q.; Huo, H.; Yao, J.-C.; Zhang, G.-M.; Zou, L.-W. *Analytical Methods* **2021**, *13*, 2671−2678.

https://doi.org/10.1021/acs.analchem.3c02909
Anal. Chem. 2023, 95, 17577−17585